Cell Reports

Article

Peripheral astral microtubules ensure asymmetric furrow positioning in neural stem cells

Graphical abstract

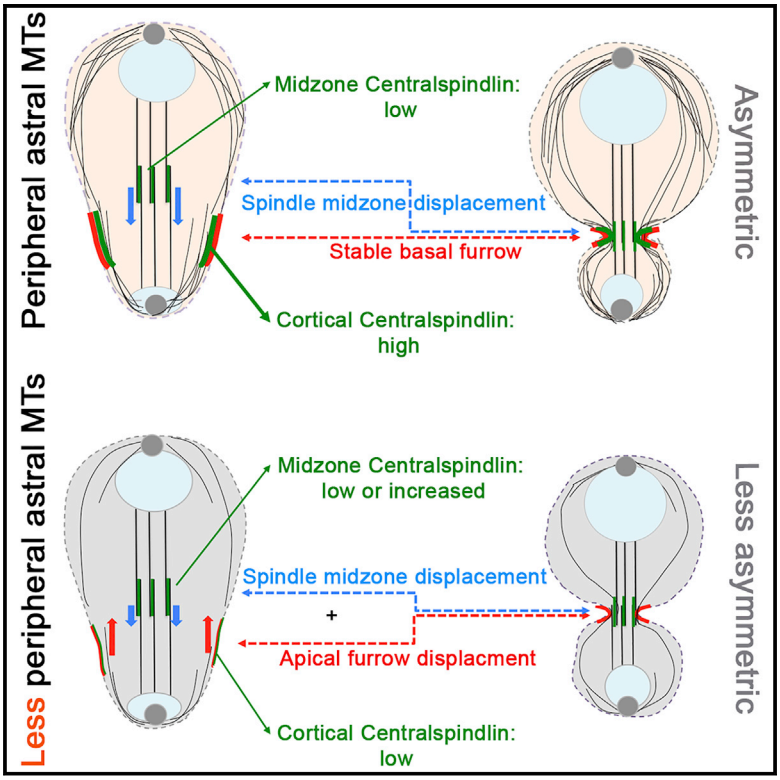

Highlights

- Midzone and cortical centralspindlin pools are spatially separated
- The cortical centralspindlin pool is dominant
- Peripheral MTs recruit the centralspindlin pool at the cortical cleavage furrow
- Midzone centralspindlin becomes dominant when astral peripheral MTs are impaired

Authors

Alexandre Thomas, Emmanuel Gallaud, Aude Pascal, ..., Laurent Richard-Parpaillon, Matthew Scott Savoian, Régis Giet

Correspondence

regis.giet@univ-rennes1.fr

In brief

Centralspindlin positions the cleavage furrow. Thomas et al. show that astral MTs target a dominant centralspindlin pool to the basal furrow in fly neuroblasts. This pool is separated from spindle-midzone-associated centralspindlin. When centralspindlin cortical recruitment is impaired, the midzone pool takes the lead to reset furrowing apically.

Thomas et al., 2021, Cell Reports *37*, 109895
October 26, 2021
https://doi.org/10.1016/j.celrep.2021.109895

CellPress

Cell Reports

CellPress
OPEN ACCESS

Article

Peripheral astral microtubules ensure asymmetric furrow positioning in neural stem cells

Alexandre Thomas,[1] Emmanuel Gallaud,[1] Aude Pascal,[1] Laurence Serre,[2] Isabelle Arnal,[2] Laurent Richard-Parpaillon,[1] Matthew Scott Savoian,[3] and Régis Giet[1,4,*]

[1]Univ Rennes, CNRS, IGDR (Institut de Génétique et Développement de Rennes) - UMR17 6290, 35000 Rennes, France
[2]Inserm U1216, CEA, CNRS, Grenoble Institut Neurosciences (GIN), Université Grenoble Alpes, 38000 Grenoble, France
[3]School of Fundamental Sciences, Massey University, 4410 Palmerston North, New Zealand
[4]Lead contact
*Correspondence: regis.giet@univ-rennes1.fr
https://doi.org/10.1016/j.celrep.2021.109895

SUMMARY

Neuroblast division is characterized by asymmetric positioning of the cleavage furrow, resulting in a large difference in size between the future daughter cells. In animal cells, furrow placement and assembly are governed by centralspindlin that accumulates at the equatorial cell cortex of the future cleavage site and at the spindle midzone. In neuroblasts, these two centralspindlin populations are spatially and temporally separated. A leading pool is located at the basal cleavage site and a second pool accumulates at the midzone before traveling to the cleavage site. The cortical centralspindlin population requires peripheral astral microtubules and the chromosome passenger complex for efficient recruitment. Loss of this pool does not prevent cytokinesis but enhances centralspindlin signaling at the midzone, leading to equatorial furrow repositioning and decreased size asymmetry. These data show that basal furrow positioning in neuroblasts results from a competition between different centralspindlin pools in which the cortical pool is dominant.

INTRODUCTION

Cytokinesis in somatic cells ensures the equal partitioning of the segregated chromosomes and is responsible for the division of the mother cell's cytoplasm into two daughters. This process requires the highly orchestrated assembly and constriction of an acto-myosin contractile ring, usually at the cell's center. The use of various model systems has clearly established that the mitotic spindle defines the position of the contractile ring and the resulting cleavage furrow (von Dassow, 2009; Rappaport, 1971). Two populations of mitotic spindle microtubules (MTs) have been shown to trigger the assembly of the contractile machinery during anaphase. The first is a subpopulation of astral MTs. These MTs emanate from the centrosomes to the equatorial cortex, where they deliver furrow-inducing signals (Foe and von Dassow, 2008; Vale et al., 2009; Shannon et al., 2005). The second population comprises the spindle midzone, a region of antiparallel MT overlap and interdigitation within the central spindle that assembles between the decondensing daughter nuclei. In many symmetrically dividing somatic cell types, the relative contribution of these two populations has been difficult to unambiguously determine due to their close proximity at the cell's equator. Yet, experiments during the last few decades have led to a proposed common mechanism across model systems in which the furrow-inducing signals emanate from both cortical proximal astral MTs and the spindle midzone, with each acting in parallel. However, these pathways do not appear to be equivalent. For instance, if the furrow is initiated at a position distal to the midzone, it will regress and a new one will be established proximal to it (von Dassow, 2009; Foe and von Dassow, 2008; Bringmann and Hyman, 2005; Mishima, 2016). Thus, in equatorially dividing cells, the spindle midzone pathway acts dominantly and can reset furrow position.

Centralspindlin is the main orchestrator of furrowing. This protein complex is a tetramer composed of two subunits of kinesin-6 (Pavarotti-klp in *Drosophila melanogaster*) and two subunits of MgcRacGAP (Tumbleweed in *D. melanogaster*). Tumbleweed is essential for the activation of Rho-GEF Ect2 (Pebble in *D. melanogaster*). The formation of Rho-GTP triggers the local activation of Rho kinase and phosphorylation of non-muscle myosin regulatory light chain, an event that stimulates myosin activation and ultimately drives cytoplasmic cleavage (D'Avino et al., 2015; Glotzer, 2017). Although it is well established that centralspindlin acts along central spindle MTs and accumulates at the cell cortex equator to promote symmetrical cleavage, far less is known about how this complex governs asymmetrical divisions. *Drosophila* neural stem cells (neuroblasts; NBs) are characterized by a biased furrow placement toward the basal region of the cell. Asymmetric cytokinesis triggers the formation of a large apically positioned cell that retains the NB identity, and a small basal ganglion mother cell (GMC) that will undergo differentiation (Knoblich, 2010). Redistribution of myosin immediately after anaphase onset is the important event that triggers asymmetric cell shape (Cabernard et al., 2010; Connell et al., 2011; Tsankova et al., 2017). Indeed, apical myosin clearing induces apical cortical expansion. This is followed by a basal clearing,

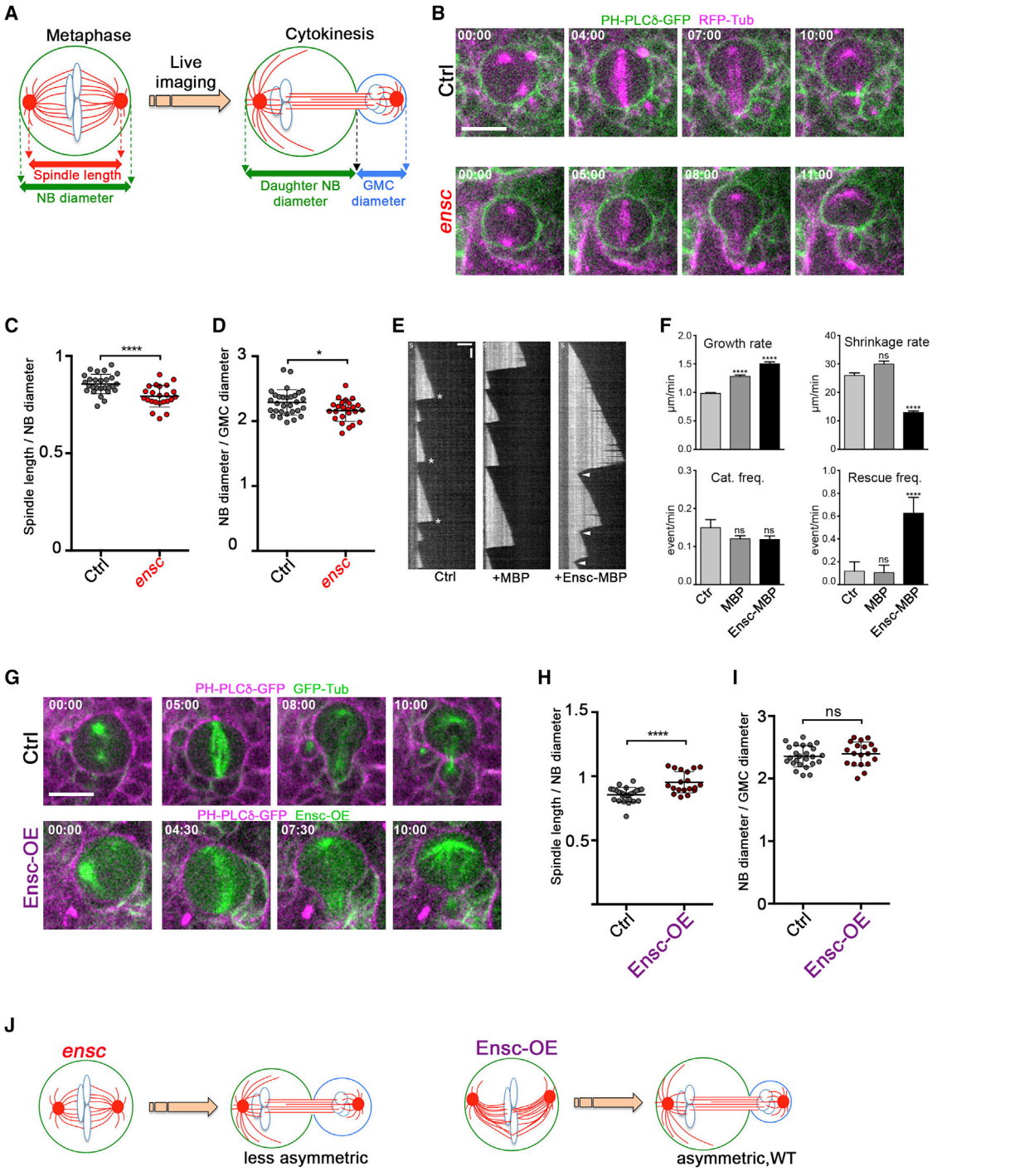

Figure 1. Analysis of cell size asymmetry in *ensc* and Ensc-OE NBs

(A) Scheme of a neuroblast (NB) during cell division during metaphase (left) and telophase (right). Note that the NB cell division is asymmetric and produces a large NB and a small ganglion mother cell (GMC) during cytokinesis.

(B) Selected images of a control NB (top) and an *ensc* mutant NB (bottom) during cell division. The membranes are displayed in green and the MTs are displayed in magenta. Time is min:s. Scale bar, 10 μm.

(C) Dot plot showing the mean (±SD) mitotic spindle length/NB diameter ratio in control (0.86 ± 0.05, n = 27) or in *ensc* NBs (0.79 ± 0.06, n = 23); ***p < 0.0001 (Mann-Whitney test).

(D) Dot plot showing the NB mean (±SD) diameter/GMC diameter ratio in control (2.29 ± 0.20, n = 27) or in *ensc* NBs (2.16 ± 0.20, n = 23); *p < 0.05 (Mann-Whitney test).

(legend continued on next page)

which similarly induces an expansion of the basal cortex. This ultimately biases the furrow toward the basal portion of the cell (Cabernard et al., 2010; Connell et al., 2011). Previous studies have shown that these two processes are under the strict control of the NB polarity machinery and influenced by the spindle midzone and the chromosome passenger complex (CPC) (Roth et al., 2015; Tsankova et al., 2017). To better understand the mechanism of furrow positioning in asymmetrical cytokinesis, we have genetically manipulated spindle size and MT dynamics in *Drosophila* NBs. Our data indicate that the mechanisms dictating asymmetrical daughter cell size are extremely robust and tolerate increases in spindle length and shape. We report that furrowing initiates in a midzone-independent manner, at a basal position through the action of a subcortical centralspindlin pool targeted by peripheral astral MTs. When these MTs are impaired, centralspindlin recruitment at the furrow is also affected and becomes abnormally enriched at the midzone, causing repositioning of the cleavage site, thus affecting the size asymmetry of the daughter cells. Together, these results reveal that unlike most systems, in *Drosophila* NBs, which are characterized by a high level of cell size asymmetry during cell division, a population of peripheral astral MTs, and not the spindle midzone, defines and maintains asymmetrical cleavage furrow positioning.

RESULTS

Cell size asymmetry is compromised following Ensconsin depletion but not overexpression in NBs

NBs divide asymmetrically to generate a large self-renewing NB and a smaller differentiating GMC (Figure 1A). We previously showed that Ensconsin is required for MT polymerization during cell division; consequently, *ensc* mutant spindles are shorter than their wild-type (WT) counterparts (Gallaud et al., 2014). To investigate the possible consequences of a change in spindle length for NB asymmetric cell division, we first analyzed, by live-cell imaging, cell size asymmetry of dividing NBs in control and *ensc* mutants (Figure 1). We confirmed the previous finding that loss of Ensconsin triggered an ~10% decrease in mitotic spindle length (Figures 1B and 1C). Strikingly, the *ensc* mutants displayed a small yet statistically significant reduction in the ratio between NB and GMC diameters, indicating a loss of asymmetry (Figures 1D and 1J, left). This defect could either result from the associated change in spindle length or indicate some uncharacterized function for Ensconsin in asymmetrical size fate determination. To further explore the role of Ensconsin in MT dynamics *in vitro*, we used total internal reflection fluorescence (TIRF) microscopy and recombinant Ensconsin protein (Figure 1E). Ensconsin-MBP (maltose-binding protein) had a small but significant effect on MT growth rate. Most striking was the ~50% reduction in the rate of MT shrinkage and the more than 3 times increase in the rescue frequency compared to controls or MBP alone (Figure 1F). In line with these results, overexpression of Ensconsin (Ensc-OE) in NBs led to elongated spindles that buckled when reaching the cortex (Figures 1G, 1H, and S1), consistent with previous work in symmetrically dividing S2 cells (Gallaud et al., 2014). Despite the increase in MT polymerization and spindle length, the level of size asymmetry remained unperturbed following cytokinesis in Ensc-OE NBs (Figures 1I and 1J, right).

Enhancement of spindle length through overexpression of Msps or depletion of kinesin-8 MT depolymerase does not alter cell size asymmetry

To determine whether daughter cell size asymmetry is insensitive to stimulation of MT growth, we quantified size asymmetry following overexpression of the MT-associated protein (MAP) Mini spindles, the fly ortholog of MAP215/ch-TOG, a protein with MT polymerization properties (Reber et al., 2013; Cullen et al., 1999; Fox et al., 2014). In parallel, we performed RNAi-mediated depletion of the MT-depolymerizing kinesin-8 fly family member Klp67A. This kinesin depolymerizes MTs and its depletion leads to the formation of exceptionally long spindles in *Drosophila* cells (Goshima et al., 2005; Edzuka and Goshima, 2019). Similar to Ensc-OE, overexpression of Msps-RFP (Msps-OE) or RNAi-mediated depletion of Klp67A led to the formation of long and bent mitotic spindles (Figures 2A, 2B, 2D, and S1A; Videos S1 and S2). Neither perturbation affected the post-cleavage asymmetric cell size (Figures 2A, 2C, and 2E). These data suggest that asymmetric cell size regulation is not sensitive to an increase in MT polymer or spindle length elongation.

Spindle shortening through overexpression of kinesin-8 or -13 MT depolymerases decreases cell size asymmetry

To investigate whether the size asymmetry reduction observed in *ensc* mutants (Figure 1) was unique to Ensconsin or rather a

(E) Kymographs showing microtubules (MTs) assembled from GMPCPP seeds and 14 μM tubulin in the absence or presence of 200 nM MBP or MBP-Ensconsin. Horizontal and vertical scale bars, 5 μm and 60 s, respectively.
(F) Graphs showing the mean (±SD) growth and shrinkage rates and the catastrophe and rescue frequencies determined from kymographs shown in (E). ns, non-significant; ****p < 0.0001 (Kruskal-Wallis ANOVA followed by post hoc Dunn's multiple comparison; total number of growth events = 116, 123, and 107; total number of shrinkage events = 67, 73, and 81; total number of catastrophe events = 94, 96, and 83; and total number of rescue events = 3, 3, and 33 for the control, MBP, and MBP-Ensconsin, respectively).
(G) Selected images of a control NB (top) and an Ensc-OE NB (bottom) during cell division. Membranes are displayed in magenta and MTs or Ensconsin are displayed in green. Time is min:s. Scale bar, 10 μm.
(H) Dot plot showing the mean (±SD) mitotic spindle length/NB diameter ratio in control (0.86 ± 0.06, n = 25) or in Ensc-OE NBs (0.95 ± 0.08, n = 19); ****p < 0.0001 (Mann-Whitney test).
(I) Dot plot showing the mean (±SD) NB diameter/GMC diameter ratio in control (2.36 ± 0.17, n = 25) or in Ensc-OE NBs (2.40 ± 0.19, n = 19); ns, non-significant (Mann-Whitney test).
(J) Summary of NB division in *ensc* (left) or Ensc-OE (right). *ensc* mutant NBs display shorter spindles and undergo less asymmetric cell division whereas Ensc-OE NBs, despite harboring long spindles, divide asymmetrically similar to WT. Time is min:s.
See also Figure S1 and Videos S1 and S2.

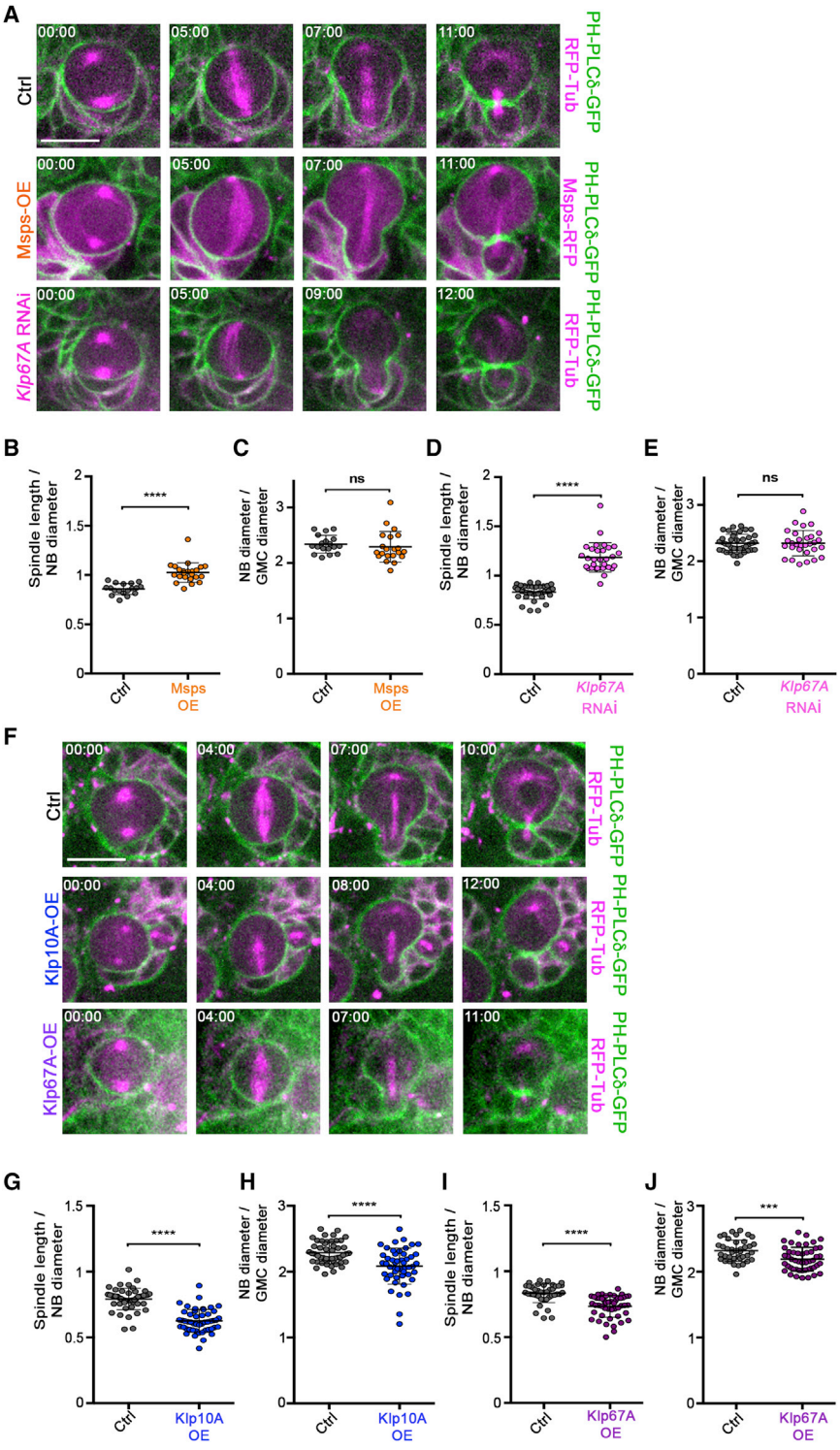

Figure 2. Analysis of cell size asymmetry in NBs following modification of several MAP levels

(A) Selected images of control (top), Msps-OE (middle), and *Klp67A* RNAi (bottom) NBs. The membranes are shown in green; the MTs (top and bottom) and Msps (middle) are shown in magenta. Time is min:s. Scale bar, 10 μm.

(B) Dot plot showing the mitotic spindle length/NB diameter ratio (±SD) in the NBs of control (0.86 ± 0.06, n = 18) or in Msps-OE transgenic flies (1.03 ± 0.1, n = 23); ****p < 0.0001 (Mann-Whitney test).

(C) Dot plot showing the mean (±SD) NB diameter/GMC diameter ratio in control (2.34 ± 0.16, n = 18) or in Msps-OE NBs (2.29 ± 0.28, n = 21); ns, non-significant (Mann-Whitney test).

(D) Dot plot showing the mean (±SD) mitotic spindle length/NB diameter ratio in control NBs (0.83 ± 0.07, n = 40) or in *Klp67A* RNAi NBs (1.19 ± 0.15, n = 30); ****p < 0.0001 (Mann-Whitney test).

(E) Dot plot showing the mean (±SD) NB diameter/GMC diameter ratio in control (2.31 ± 0.16, n = 40) or in *Klp67A* RNAi NBs (2.32 ± 0.23, n = 30); ns, non-significant (Mann-Whitney test).

(F) Selected images of control (top), Klp10A-OE (middle), and Klp67A-OE (bottom) NBs. The membranes are shown in green; the MTs are shown in magenta. Scale bar, 10 μm. Time is min:s.

(G) Dot plot showing the mean (±SD) mitotic spindle length/NB diameter ratio in control NBs (0.79 ± 0.08, n = 49) or in Klp10A-OE NBs (0.63 ± 0.09, n = 49); ****p < 0.0001 (Mann-Whitney test).

(H) Dot plot showing the NB diameter/GMC diameter ratio (±SD) in control NBs (2.29 ± 0.17, n = 49) or in Klp10A-OE NBs (2.00 ± 0.27, n = 49); ****p < 0.0001 (Mann-Whitney test).

(I) Dot plot showing the mean (±SD) mitotic spindle length/NB diameter ratio in control NBs (0.83 ± 0.07, n = 40) or in Klp67A-OE NBs (0.73 ± 0.08, n = 48); ****p < 0.0001 (Mann-Whitney test).

(J) Dot plot showing the mean (±SD) NB diameter/GMC diameter ratio in control NBs (2.32 ± 0.16, n = 40) or in *Klp67A* RNAi NBs (2.19 ± 0.18, n = 48); ***p < 0.0001 (Mann-Whitney test).

See also Figure S1 and Video S3.

common effect of spindle shortening, we induced other perturbations of MT polymerization by overexpressing two MT-depolymerizing kinesins: either Klp10A, which belongs to the kinesin-13 family (Klp10A-OE), or the kinesin-8 member Klp67A (Klp67A-OE) (Figure S1A). Importantly, whereas the depletion of either causes spindle elongation, their overexpression results in abnormal shortening (Laycock et al., 2006; Morales-Mulia and Scholey, 2005; Radford et al., 2012; Goshima et al., 2005; Buster et al., 2007). As predicted, both Klp10A-OE and Klp67A-OE NBs exhibited shorter spindles, although the length reduction was more pronounced in Klp10A-OE cells (Figures 2F, 2G, and 2I; Video S3). Depending on the spindle's length, it assumed a lesser or greater displacement relative to the cell center. Interestingly, in these shortened spindle cells, like with *ensc* mutants, we found that the NB/GMC diameter ratio was significantly impaired, indicating that cell division was more symmetric compared to controls

(Figures 2H and 2J). Thus, defective MT polymerization leading to spindle shortening due to loss of Ensconsin function or overexpression of kinesin-8s and -13s biases asymmetric cell division. An examination of whole-brain phenotypes revealed that *ensc* mutant brain lobes did not undergo any reduction in NBs. By contrast, overexpression of either Klp67A (Figure S1B) or Klp10A triggered a moderate decrease of NBs (Figure S1C). This diminished NB number was associated with aneuploidy and polyploidy (Figures S1D and S1E). Moreover, we noticed an elevation in cell-cycle duration following Klp67A-OE cells (Figure S1F). Together, our data suggest that spindle shortening after Klp10A or Klp67A overexpression compromises cell size asymmetry but also triggers chromosome segregation errors and a loss of NBs.

Defective MT growth leads to an apical shift of the basal cleavage furrow after anaphase onset

In asymmetrically dividing NBs, it was previously demonstrated that polarity- and spindle-dependent pathways ensure appropriate myosin distribution to siblings of different sizes (Cabernard et al., 2010; Roubinet et al., 2017; Tsankova et al., 2017). These two pathways regulate the time between apical and basal myosin clearing and the subsequent apical and basal cortical expansions (Figure S2A). To investigate the behavior of the furrow, we monitored the dynamics of the regulatory light chain of myosin in live NBs using Sqh-GFP (Royou et al., 2002). In control cells, we confirmed that myosin-GFP was uniformly present at the cell cortex before anaphase (Figure 3A; Video S4). In *ensc*, Klp67A-OE, and Klp10A-OE NBs, the polarity-dependent apical and basal expansion ratios were similar to controls (Figures S2B and S2C). In metaphase NBs with these same genotypes, the cortical polarity appeared unaffected, as judged by the presence of strong aPKC and Miranda crescents at the apical and basal cortices, respectively, similar to controls Figure S2G. We also examined the polarity-dependent cleavage-furrow-positioning pathway during anaphase transition, which results in apical clearing of myosin. We found that the polarity-dependent apical myosin clearing time was not significantly changed compared to controls (Figure S2D). We did note a slight dilation in the basal myosin clearing and the time between apical and basal clearing in *ensc* and Klp10A-OE cells (Figures S2E and S2F).

We next analyzed furrow positioning through curvature measurements of the cell membrane (Tsankova et al., 2017) (Figure 3A and 3B). Whereas the furrow position remained stably placed from anaphase until cytokinesis in control NBs, we found it shifted significantly toward the apical side during completion of cell division in *ensc* and Klp67A-OE cells, with a maximal displacement observed for Klp10A-OE NBs (Figure 3C; Videos S5 and S6). Whereas the furrow width was consistently ~10% of the half-cell cortex length in control NBs as revealed by myosin-GFP (Figures 3D and 3E), the signal occupied a larger space in *ensc* and Klp67A-OE NBs, with the maximum width of ~25% of the half-cell cortex length observed for Klp10A-OE cells at comparable time points (Figures 3A and 3E; Video S6). From this, we conclude that proper MT growth is required following action of the polarity pathway for maintaining furrow size and position during asymmetric cell division.

Centralspindlin is spatially and temporally regulated as two distinct populations

Our previous perturbations, which interfered with MT dynamics, suggested that a common mechanism was at play for maintaining the furrow position. In higher eukaryotes, myosin recruitment and activation at the cleavage furrow are regulated by the highly conserved centralspindlin complex, a tetramer composed of a kinesin-6 family member complexed with MgcRacGAP (Pavarotti-klp and Tumbleweed in *Drosophila*, respectively) (D'Avino et al., 2005, 2015; Mishima, 2016). Strikingly, we found that the combination of Klp10A-OE and a single copy of the pav^{B200} null allele enhanced the asymmetry defect observed with Klp10A-OE alone (Figure S2H). Centralspindlin functionality and targeting to the membranes is regulated by the CPC-dependent oligomerization (Basant et al., 2015). We therefore challenged the complex by introducing a single null allele for its Survivin subunit, svn^{2180}, and monitored the effects on cell symmetry in the Klp10A-OE background. We found that Klp10A-OE-dependent size asymmetry defects were further enhanced when Survivin levels were reduced (Figure S2H). These results suggest that the observed asymmetry defects are due, at least in part, to impaired centralspindlin function.

In most eukaryotic cells, the centralspindlin complex is located at the spindle midzone and at the equatorial cortex. To characterize the furrow mis-positioning that accompanies defective MT growth, we analyzed the spatiotemporal distribution of the motor component of centralspindlin, Pavarotti-klp, in different experimental backgrounds. We began by examining GFP-Pav-klp (Minestrini et al., 2003) localization in control NBs. Our time-lapse studies showed that most of the GFP-Pav-klp was located at the cortex at the cleavage site (Figures 4A, 4E, and S3A). Following the onset of furrow ingression, a second pool started to accumulate into a small and spatially distinct band near the former site occupied by the metaphase chromosomes at the spindle midzone (Figures 4A and S3A; Video S7). The spatial and temporal separation of the GFP-Pav-klp signals led us to speculate that these were separate pools of centralspindlin. To confirm this hypothesis, we tracked GFP-Pav-klp in cells lacking MTs that were forced into anaphase using *Mad2* RNAi to abrogate the spindle assembly checkpoint (Gallaud et al., 2014). Under these conditions, GFP-Pav-klp showed a slight enrichment at the basal cortex but this pool remained at almost baseline levels compared to control cells, which showed continuous cortical recruitment of GFP-Pav-klp following anaphase onset (Figures S3B and S3C). When MT polymerization was impaired in *ensc*, Klp10A-OE, and Klp67A-OE cells, even if the centralspindlin component GFP-Pav-klp was initially present at the equatorial cell cortex, it did not become enriched at the cleavage site to the levels measured in controls (Figures 4B, 4C, and 4E, red arrowheads, and S4A; see also Videos S8 and S9). Instead, in Klp10A-OE (Video S9), Klp67A-OE, but not in *ensc* NBs (Video S8), GFP-Pav-klp was more abundant at the spindle midzone (Figures 4B and 4C, time 100 s blue arrows and insets at time 180 s, 4E, and S4B). Together, these experiments reveal that centralspindlin exists as two distinct and separable populations, one at the basal cortex and one at the spindle midzone. The decrease of the cortical centralspindlin pool is always accompanied by a displacement of the cleavage furrow.

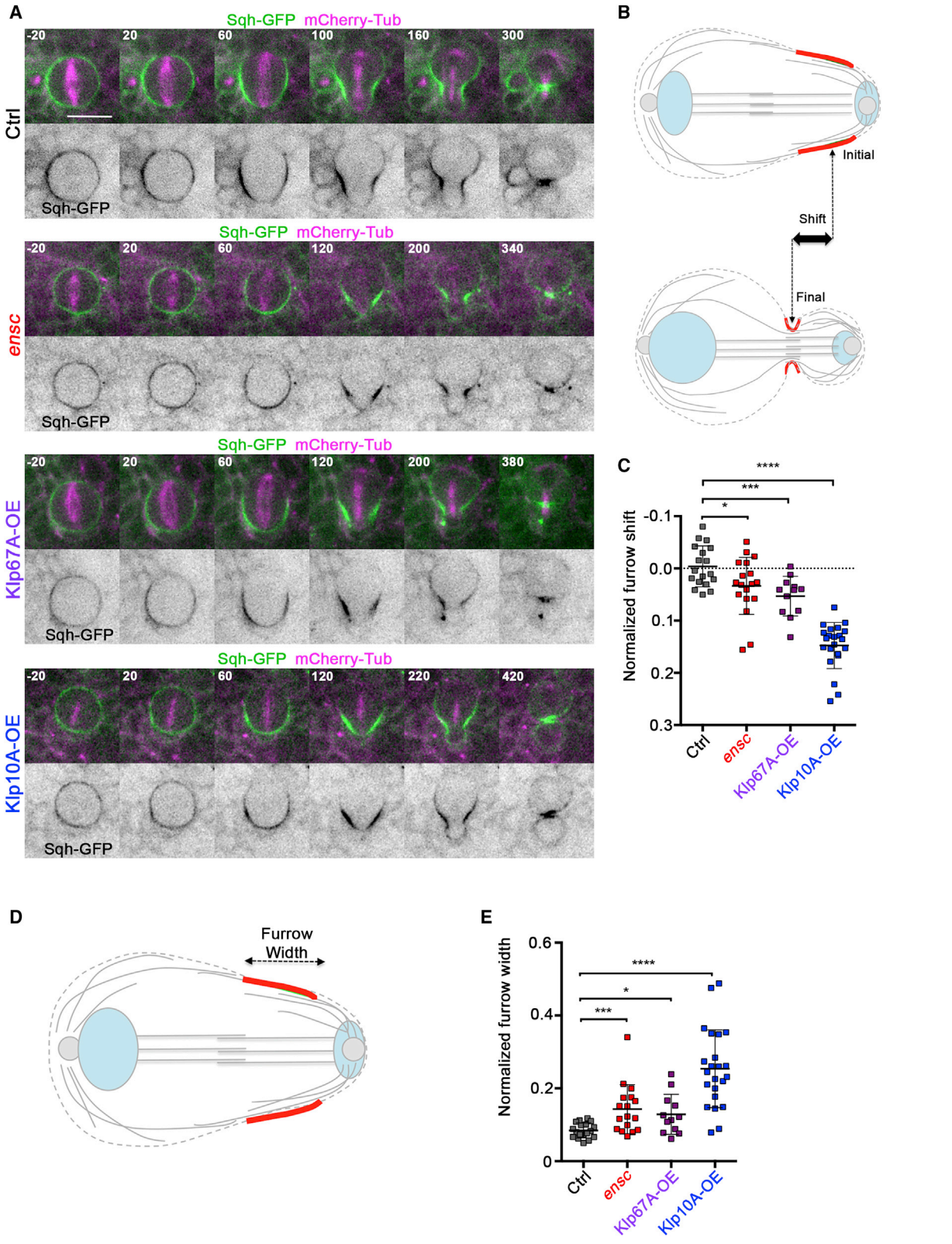

(legend on next page)

The spatiotemporal regulation of centralspindlin relies on stable peripheral MTs

Fluorescence quantification (Figure 4F) revealed that compared to controls, Klp10-OE and Klp67A-OE NBs both displayed a decrease in cortical GFP-Pav-klp signal with a concomitant increase at the midzone (Figure S4). To further characterize the relationship between cortical and midzone centralspindlin pools and the role of MT growth in asymmetrical cleavage, we examined GFP-Pav-klp dynamics in *sas-4*^{s2214} mutants, which retain an active polarity pathway but lack centrosomes and their associated astral MTs (Cabernard et al., 2010; Basto et al., 2006). In this background, cortical enrichment also appeared diminished relative to the midzone (Figures 4D, S4A, and S4B). An enlarged view of the boxed regions for 180-s post-anaphase onset highlights this increased centralspindlin recruitment at the spindle midzone and weaker accumulation at the cell cortex (Figure 4E). Although *sas-4*^{s2214} NBs exhibited signal enrichment at their midzones, not all cells had a clear cortical reduction (Figure S4). In addition, *sas-4*^{s2214} mutants exhibited both an increased spindle length as well as a significant overall cell size asymmetry defect (Figures S5A and S5B), further supporting the idea that MT-asters maintain a basal furrow position. Similar to previous studies, the cortico-basal expansion ratios were unchanged in *sas-4*^{s2214} NBs (Connell et al., 2011). This indicates that the centrosome-associated MT-asters are also important for furrow positioning (Figure S5D). To confirm the contribution of MT-asters in furrow positioning and maintenance, we removed them through laser ablation of the apical and basal centrosomes. Each centrosome was labeled with GFP-tagged Aurora A and apical and basal centrosomes were irradiated by a multi-photon laser until the signal was no longer detectable. Sample fixation and immunostaining after laser ablation showed the complete disappearance of the Cnn-labeled centrosome and its associated astral MT-aster (Figure S5E, arrowhead). Consistent with centrosome removal, ablated cells displayed a phenotype virtually identical to *sas-4*^{s2214} mutants: daughter cells exhibited diminished cell size asymmetry after the ensuing cytokinesis (Figures S5F and S5G; Video S10, compare left and right). These live-cell observations suggested that astral MTs were essential to cleavage furrow positioning. Accurate quantification of MTs in live cells was precluded by the lack of spatial resolution in our recordings. We therefore performed a quantitative analysis of fixed preparations. Although fixed-cell approaches can introduce unintentional bias due to different substage durations that can mask subtle MT dynamic changes, large-scale trends and differences will be preserved. Detailed morphological examination revealed that in control NBs, bundles of astral MTs were closely apposed to the cortex at the cleavage furrow. This was not the case with *ensc*, Klp67A-OE, or Klp10-OE NBs, all of which showed decreased MT densities and lacked the presumptive bundles (Figures S5H and S5I). Taken together, our data strongly suggest that peripheral astral MTs originating from the apical and basal centrosomes play a key role in inducing asymmetric cell division.

Depletion of the spindle midzone protein Feo does not trigger furrow-positioning defects

The presence of GFP-Pav-klp at the spindle midzone distal to the cleavage site and the movement of the furrow toward the equator in peripheral MT-deficient cells prompted us to further characterize the cleavage site and the spindle midzone in control cells. For this purpose, we used Fascetto-GFP (the homolog of the mammalian PRC1 protein; Feo-GFP), a marker that uniquely labels the spindle midzone (Figure 5A) (Vernì et al., 2004; Wang et al., 2015). We found that in these NBs the metaphase plate was slightly shifted toward the basal side relative to the cell equator along the apico-basal axis (Figures 5A, time −120 s, blue arrowhead, and 5C, left) but similarly placed to the midzone-defining Feo-GFP signal that appears following anaphase chromosome segregation (Figures 5A, time 60 s, 5B, and 5C, middle). This was in contrast to the position of the cleavage furrow (Figures 5A, time 90, compare green and red arrowheads, 5B, and 5C, right), which was always distinct and basally distal to the midzone (Figure 5D; Video S11). Kymograph analyses of the spindle midzone and cell membranes revealed that the midzone moves basally during the ingression of the furrow until they ultimately consolidate into a single structure (Figure 5B). These distribution data raise the possibility that Feo and the spindle midzone may not contribute to furrow positioning in WT NBs. We therefore assayed whether Feo depletion and spindle midzone destabilization could impair furrow positioning and asymmetric cell division. We found that Feo-depleted NBs (Figure 5E) did not exhibit furrow-positioning defects during anaphase (Figures 5F and 5G) and the final NB/GMC diameter ratio was similar to controls (Figure 5H). However, 22% (4/18) of Feo-depleted NBs exhibited late cytokinesis failure (Figure S6A). Thus, spindle midzone MTs appear to play a key role during the late steps of cytokinesis rather than in furrow positioning during anaphase. In parallel, we analyzed whether the midzone was reinforced following astral MT depletion (Figures 5I, 5J, and S6B). The Feo-GFP signal intensity at the midzone was enhanced in Klp10A-OE NBs (Figures 5I and S6C) but remained unchanged in Klp67-OE and

Figure 3. Analysis of myosin dynamics and furrow positioning in *ensc*, Klp67-OE, and Klp10A-OE NBs

(A) Selected images of (from top to bottom) dividing control, *ensc*, Klp67A-OE, and Klp10A-OE NBs expressing tubulin (magenta) and myosin regulatory light chain (green and lower panels in monochrome) after anaphase onset (t = 20 s) until late telophase. Scale bar, 10 μm. Time is s.

(B) Scheme showing the possible apical shift between the initial and final furrow curvature analyses.

(C) Dot plot showing the mean (±SD) of the relative furrow displacement between early anaphase and late telophase in control (0.00 ± 0.04, n = 18), *ensc* (−0.03 ± 0.05, n = 18), Klp67A-OE (−0.05 ± 0.04, n = 12), and Klp10A-OE NBs (−0.14 ± 0.04, n = 22); *p < 0.05, ***p < 0.001, ****p < 0.0001 (Mann-Whitney test).

(D) Scheme showing the furrow width (red) during mid-anaphase.

(E) Dot plot showing the mean (±SD) relative myosin furrow width/cell length ratio for control (0.08 ± 0.02, n = 18), *ensc* (0.14 ± 0.07, n = 17), Klp67A-OE (0.13 ± 0.05, n = 12), and Klp10A-OE NBs (0.25 ± 0.11, n = 23); *p < 0.05, ***p < 0.001, ****p < 0.0001 (Mann-Whitney test).

See also Figure S2 and Videos S4, S5, and S6.

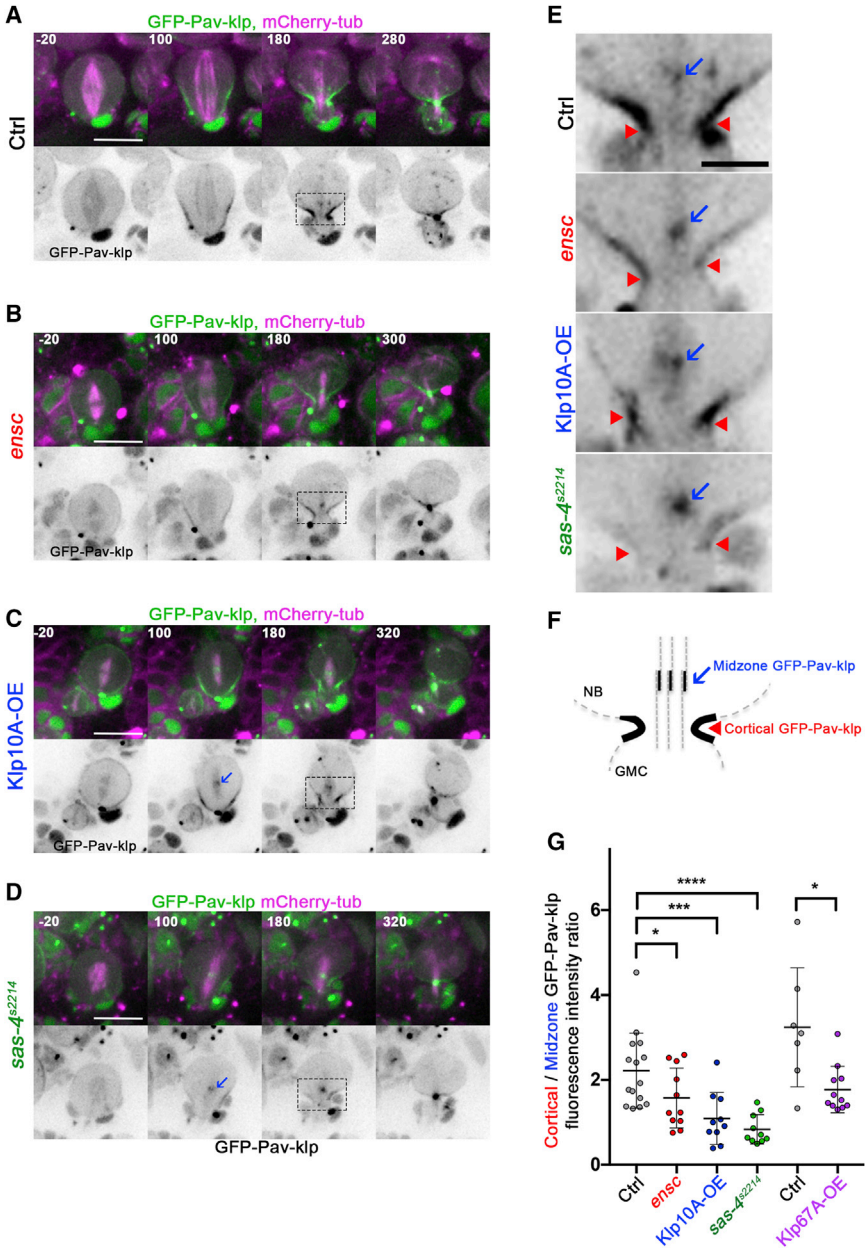

Figure 4. Analysis of centralspindlin localization and dynamics in control, *ensc*, Klp10A-OE, and *sas-4*^{s2214} NBs

(A) Selected images of dividing control expressing tubulin (magenta) and GFP-Pav-klp (green and lower panels in monochrome) from anaphase onset until late telophase (top left).

(B) *ensc* NB.

(C) Klp10A-OE NB.

(D) *sas-4*^{s2214} NB (bottom).

Scale bars, 10 μm. Time is s.

(E) Higher-magnification view of the selected control, *ensc*, Klp10A-OE, and *sas-4*^{s2214} telophase NBs (from A–D) showing GFP-Pav-klp localization at the cleavage site. See the strong signal at the cell cortex (red arrowheads) and the weak signal at the presumptive spindle midzone away from the cleavage site, toward the apical side (blue arrows). Scale bar, 3.5 μm.

(F) Scheme of the cleavage site showing the cortical and midzone centralspindlin pools.

(G) Dot plot showing the mean (±SD) relative cortical/midzone GFP intensity ratio for control (2.21 ± 0.89, n = 15), *ensc* (1.57 ± 0.70, n = 11), Klp10A-OE (1.09 ± 0.61, n = 10), *sas-4*^{s2214} (0.84 ± 0.35, n = 10), control (3.24 ± 1.40, n = 7), and Klp67A-OE NBs (1.77 ± 0.55, n = 11); *p < 0.05, ***p < 0.001, ****p < 0.0001 (Mann-Whitney test). See also Figures S3–S5 and Videos S7, S8, S9, and S10.

sas-4^{s2214} NBs. In addition, the signal was decreased in *ensc* mutant NBs (Figure S6C). Moreover, the spindle midzone signal was significantly longer in *ensc*, Klp10A-OE, Klp67-OE, and *sas-4*^{s2214} NBs (Figure S6D). Interestingly, we also observed that mitotic spindle length was restored after metaphase and was similar to telophase controls in Klp10A-OE NBs (Figure S6E). In these NBs, furrow displacement toward the apical cortex was accompanied by a reduced midzone movement toward the basal cortex (Figure S6F). In summary, these data demonstrate that the spindle midzone in NBs occupies a spatially different position from that of the furrow and its associated cortical MTs. Both of these MT structures can recruit centralspindlin; however, under normal circumstances in *Drosophila* NBs, it is the cortical pool that dominates to define the cleavage site (Figure S6G).

DISCUSSION

Asymmetric cell division is a robust process that ensures that two daughter cells inherit different fates and sizes. The *Drosophila* NB is a powerful and widely used model system to study this specialized form of division (Rusan and Peifer, 2007; Januschke and Gonzalez, 2008; Rebollo et al., 2007). In this study, we have challenged asymmetric cell division by modifying MT growth dynamics. We were able to increase mitotic spindle length using overexpression of MT-polymerizing MAPs (Msps and Ensconsin), as well as by RNAi-mediated depletion of Klp67A, a member of the kinesin-8 family of MT-depolymerizing kinesins. Despite the presence of long and bent mitotic spindles under these conditions, the NB cell size ratio remained unchanged relative to control NBs. This reveals that asymmetric cell division and asymmetric positioning of the cleavage furrow are resistant to an excess of abnormally long and stable MTs during cell division. By contrast, decreasing MT stability and shortening the mitotic spindle produced more symmetric cell divisions. This change was due to an apical shift of the cleavage furrow during its ingression, following apical and basal cortex expansion. This phenotype was not MAP dependent and was

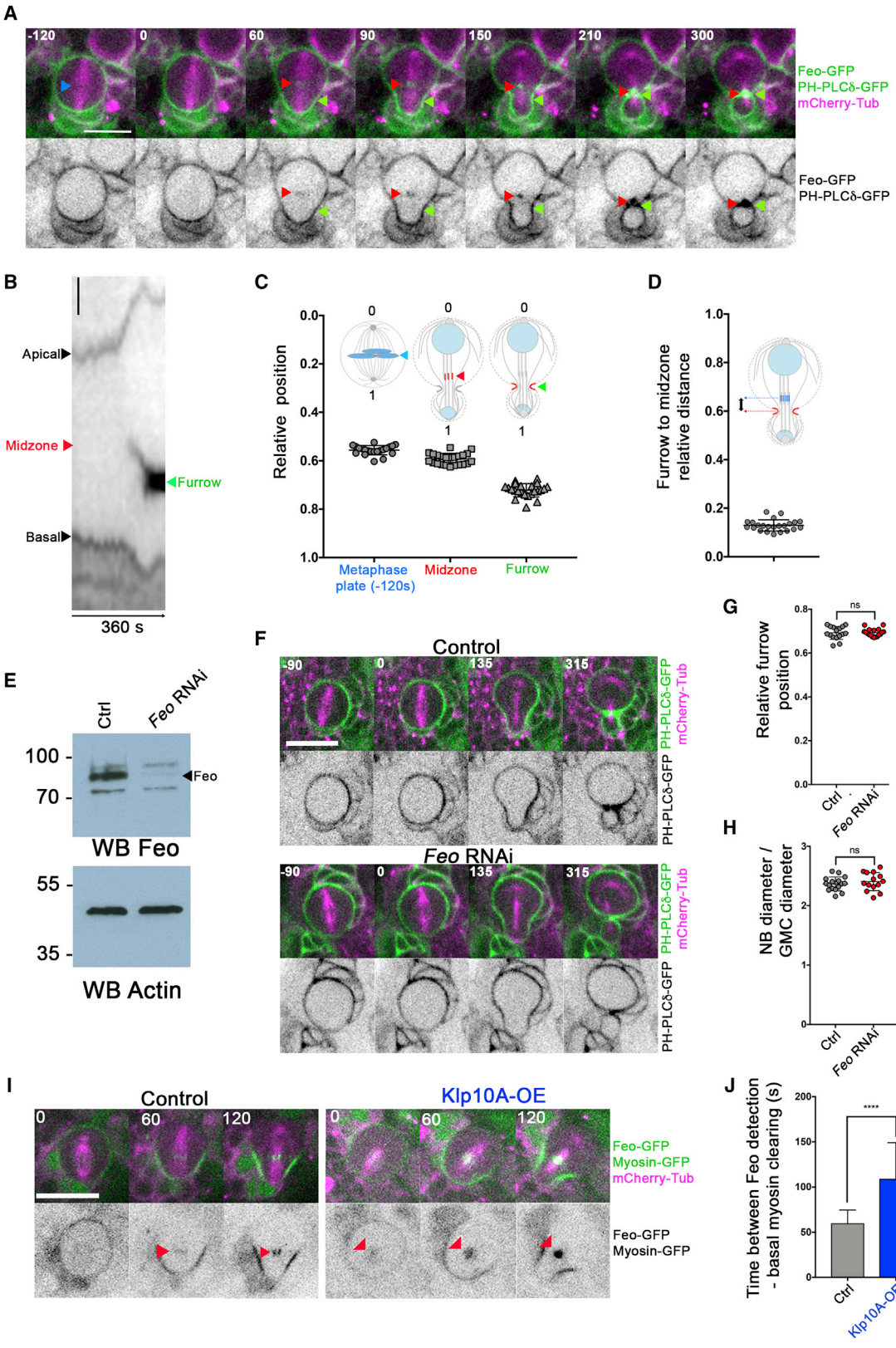

(legend on next page)

observed following overexpression of either Klp10A (kinesin-13) or Klp67A (kinesin-8) MT depolymerases and in *ensc* mutants. Rather, the data suggest that spindle size or interference with MT dynamics is responsible for the phenotype. In agreement with this, spindle size is restored in Klp10A-OE telophase cells, which display the shortest spindles at metaphase (Figure S6E). Interestingly, *sas-4*^{s2214} mutants, which are reported to lack functional centrosomes and thus astral MTs, yielded reduced levels of cell size asymmetry despite harboring longer metaphase spindles (Basto et al., 2006). This suggests that MT-asters and not spindle length are the key determinant factor for size asymmetry in NBs. Consistent with this, loss of either apical or basal MT-asters, through targeted laser irradiation and ablation prior to anaphase onset, also reduced sibling cell size asymmetry. Together, these results strongly suggest that astral MTs are required to maintain a cleavage site, which normally favors a basal position in the fly NB. We propose that a specific population of these astral MTs, called peripheral MTs, is positioned in direct contact with the division furrow and plays a determining role in maintaining its stable position during anaphase until cytokinesis. For technical reasons, we were unable to quantify peripheral MT bundles in live dividing cells. However, fixed-cell analyses, despite a possible bias in the determination of late-anaphase substages, support this and revealed a significant decrease in peripheral MTs in *ensc*, Klp10A-OE, and Klp67A-OE NBs (Figure S5). Our results are in accord with reports indicating that a subpopulation of these stable astral MTs plays a key role in the initiation of furrowing in symmetrically dividing cells and that, in some systems, furrowing can occur without the presence of a stable central spindle (Murthy and Wadsworth, 2008; Foe and von Dassow, 2008; Strickland et al., 2005; Canman et al., 2003; Inoue et al., 2004; Bringmann and Hyman, 2005; Kotýnková et al., 2016; Mishima, 2016). However, in contrast to previous studies, our data reveal that in asymmetrically dividing control NBs, the astral MT-furrowing pathway dominates over the midzone pathway. Prior investigations indicated that NBs have two genetically separable pathways to drive cytokinesis. The first, the polarity-dependent pathway, triggers the clearing of apical myosin, resulting in apical cortical expansion. Interference with this pathway leads to simultaneous apical and basal clearing, symmetrical cortex expansion, equatorial furrow positioning, and symmetric division (Cabernard et al., 2010; Roth et al., 2015; Connell et al., 2011). The second, the spindle pathway, is proposed to rely on the spindle midzone and the CPC. This triggers the subsequent basal myosin clearing and basal cortical expansion (Roth et al., 2015) (Figure S2A). Several of the results presented here led us to propose another mechanism for furrow positioning that would rely on peripheral astral MTs with a minor contribution from the spindle midzone. This is supported by several of our observations. (1) Live-cell imaging and analyses utilizing GFP-Pav-klp as a marker of centralspindlin position revealed that this master controller of cytokinesis accumulated at the basal cortex throughout the entire furrow ingression process (this paper and Cabernard et al., 2010). (2) Centralspindlin levels were low at the midzone during furrow placement and ingression compared to the cortex (Figure 4). (3) We consistently found that the midzone, as defined independently using both GFP-Pav-klp and Feo-GFP, was spatially independent from the furrowing site (Figures 4, 5, and S3). Moreover, inhibition of midzone formation through Feo depletion did not impair furrow positioning but did interfere with the late stages of cytokinesis. (4) The midzone consistently relocated from an initial location to a final position that was coincident with the furrow. The converse was never observed (Figure 5B), confirming previous observations made in embryonic NBs (Kaltschmidt et al., 2000). (5) Finally, genetic or photo-based interference with centrosomes precluded astral MT formation and interaction with the cortex. Accordingly, the cortical centralspindlin pool was diminished and NBs exhibited a size asymmetry defect (Figures 4 and S4).

Our localization studies suggest that, under normal conditions, midzone-associated centralspindlin does not perform a key role in positioning of the cleavage site and that this function is served by the more abundant centralspindlin pool associated with the cortex

Figure 5. Analysis of the spindle midzone and the cleavage furrow position in brain NBs during cell division

(A) Selected images of a WT NB expressing Feo-GFP (green and lower panels in monochrome), MTs (magenta), and membranes during cell division (green and lower panels in monochrome). The metaphase plate is indicated by a blue arrowhead (−120 s). Red arrowheads indicate the spindle midzone, and the furrow is indicated by green arrowheads (60–300 s). Scale bar, 10 μm. Time is s.

(B) Kymograph showing the localization of the spindle midzone and the cell contours during the time course of the NB cell division shown in (A), along the apico-basal axis. Vertical scale bar, 5 μm.

(C) Dot plot showing the mean (±SD) relative metaphase plate position along the apico-basal cortex 90 s after anaphase onset (left: 0.56 ± 0.02, n = 21), the mean (±SD) relative spindle midzone position along the apico-basal cortex 90 s after anaphase onset (middle: 0.59 ± 0.02, n = 23), and the mean (±SD) relative furrow position along the apico-basal cortex 90 s after anaphase onset (right: 0.72 ± 0.13, n = 23).

(D) Dot plot showing the mean (±SD) relative distance between the furrow and the spindle midzone 90 s after anaphase onset (0.13 ± 0.02, n = 23).

(E) Western blot of Feo (top) and actin (bottom) protein levels in control or *Feo* RNAi brains.

(F) Control (top) or *Feo* RNAi NBs expressing PH-PLCδ-GFP (green and bottom panels in monochrome) and mCherry-tubulin (magenta). Scale bar, 10 μm. Time is s.

(G) Dot plot showing the mean (±SD) relative midzone position for control (0.69 ± 0.03, n = 16) and *Feo* RNAi NBs (0.69 ± 0.02, n = 18); ns, non-significant (unpaired t test).

(H) Dot plot showing the mean (±SD) NB/GMC size ratio for control (2.36 ± 0.12, n = 16) and *Feo* RNAi NBs (2.40 ± 0.15, n = 14). Note late cytokinesis failed in 4/18 NBs (22%); ns, non-significant (unpaired t test).

(I) Selected frames of a control (top) or a Klp10A-OE NB expressing Feo-GFP (green and bottom panels in monochrome) and mCherry-tubulin (magenta) after anaphase onset (0 s). Arrowheads indicate midzone-associated Feo-GFP. Scale bar, 10 μm. Time is s.

(J) Dot plot showing the mean (±SD) time (s) between Feo-GFP detection on the midzone and basal myosin clearing in control (59.4 ± 15.4, n = 18) and Klp10A-OE (108.7 ± 40.5, n = 15) NBs; ****p < 0.0001 (Mann-Whitney test).

See also Figure S6 and Video S11.

at the cleavage site. When peripheral astral MTs were impaired, centralspindlin enrichment at the furrow was often diminished, and in some cases was accompanied by an increase in the midzone-associated pool, leading to a decreased midzone/furrow centralspindlin ratio and a reset of the furrowing toward the equatorial midzone. This indicates that the two populations of centralspindlin are competent to signal furrowing but that the cortical pool delivered by astral MTs may be dominant. Thus, the spatial localization and the cortical/midzone ratio of centralspindlin are the pivotal determinants of final furrow position in the *Drosophila* NB. Interestingly, a recent study has shown that a similar competition between centralspindlin pools also occurs in human cells, revealing an evolutionary conservation of the mechanism (Adriaans et al., 2019). As with human cells, we found that CPC activity seems essential in this regulatory event (Figure S2C).

In contrast to a recent study in the symmetrically dividing S2 cells, we do not observe GFP-Pav-klp labeling at the plus ends of astral MTs (Vale et al., 2009; Verma and Maresca, 2019) even when studied by enhanced-resolution imaging methods. Instead, we consistently find that centralspindlin coats the entire length of astral MTs emanating from both centrosomes, suggesting that the plus-end-directed motor activity of Pav-klp is used to bring centralspindlin to the furrow in *Drosophila* NBs, similar to findings in early embryos (Minestrini et al., 2002, 2003). It is therefore likely that centralspindlin, depending on the cell type, utilizes preferentially EB1-mediated MT plus ends or the motor activity of Pav-Klp to reach the cleavage site.

In total, our data suggest a model in which competition between different centralspindlin populations is a key determinant of asymmetric division in *Drosophila* NBs. The consecutive actions of the polarity-dependent cleavage-furrow-positioning pathway and the MTs emanating from the asters serving as centralspindlin delivery arrays are essential in the whole process. In this system, we propose that the ability of the spindle midzone to define furrow and cleavage location may only become engaged during late telophase or after subcortical astral MTs are compromised. Despite their clear role in governing size asymmetry, we have not been able to induce complete daughter cell size equality through any of a host of MT-perturbing treatments. It is possible that the few MTs that remain after our perturbations are sufficient to target enough cortical centralspindlin to provide some degree of asymmetry. However, additional mechanisms, such as MT initial asymmetric midzone position and displacement toward the cleavage site, also appear important to secure a minimal level of asymmetry in these cells (Figure S6G). Elucidating these systems and their advantages for asymmetrically dividing stem cells will be important directions for future investigations on tissue homeostasis.

Limitation of this study

Our study reveals a critical role for astral MTs in maintaining the asymmetric position of the cleavage site during cytokinesis in neural stem cells. This is essential to preserve an appropriate NB/GMC size ratio. We find that the perturbation of peripheral astral MTs and the subsequent loss of asymmetry occur in the presence of a timely apical myosin clearing, an event regulated by the polarity-dependent pathway that controls apical cortical expansion during anaphase. However, we cannot fully rule out that our observations are completely polarity independent. Other additional yet uncharacterized polarity-dependent mechanisms could be involved to contribute to our findings. Indeed, it remains possible that polarity proteins participate in the regulation of other components including centrosomal or MT-associated proteins, to control the dynamics of these peripheral astral MTs and ultimately basal furrow positioning.

STAR★METHODS

Detailed methods are provided in the online version of this paper and include the following:

- KEY RESOURCES TABLE
- RESOURCE AVAILABILITY
  - Lead contact
  - Materials availability
  - Data and code availability
- EXPERIMENTAL MODELS AND SUBJECT DETAILS
- METHOD DETAILS
  - Molecular biology
  - Production of recombinant proteins
  - TIRF microscopy and analysis of MT dynamics
  - Antibodies and western blotting
  - Live-cell microscopy
  - Photo-ablation experiments
  - Live-cell imaging analysis
  - Immunofluorescence analysis
- QUANTIFICATION AND STATISTICAL ANALYSIS
  - Quantification of peripheral MTs in fixed NBs during mid-anaphase
  - Statistical analysis

SUPPLEMENTAL INFORMATION

Supplemental information can be found online at https://doi.org/10.1016/j.celrep.2021.109895.

ACKNOWLEDGMENTS

We thank Gregory Rogers, Pier Paolo d'Avino, Renata Basto, Gohta Goshima, Jordan Raff, Hiro Ohkura, Anne Royou, Roger Karess, Christian Dahmann, Antoine Guichet, Juliette Mathieu, Jean-René Huynh, Clemens Cabernard, and Tri Pham for providing fly stocks, antibodies, and complementary DNAs (cDNAs) and useful advice. We thank Chloé Rauzier for preliminary functional analyses of Ensc-OE and Msps-OE NBs. This work was funded by the Ligue Nationale contre le Cancer and the Fondation ARC pour la Recherche sur le Cancer. A.T. is a doctoral fellow of the Région Bretagne and the Ligue Nationale contre le Cancer. E.G. is a post-doctoral fellow of the Fondation pour la Recherche Médicale (DEQ20170336742). We thank the Photonic Imaging Center of the Grenoble Institute of Neurosciences, which is part of the ISdV core facility. We thank Xavier Pinson, Stéphanie Dutertre, and Sébastien Huet for advice and help with the microscopes and the Microscopy Rennes Imaging Center platform. We thank Romain Gibeaux, Pier Paolo d'Avino, and Christelle Benaud for ideas, critical readings, and helpful suggestions.

AUTHOR CONTRIBUTIONS

Conceptualization, A.T. and R.G.; methodology, A.T., E.G., I.A., and R.G.; investigation, A.T., A.P., E.G., L.S., I.A., and R.G.; writing – original draft, A.T. and R.G.; writing – review & editing, A.T., E.G., M.S.S., and R.G.; funding acquisition, R.G.; resources, R.G.; supervision, L.R.-P. and R.G.

DECLARATION OF INTERESTS

The authors declare no competing interests.

Received: September 10, 2020
Revised: February 26, 2021
Accepted: October 6, 2021
Published: October 26, 2021

REFERENCES

Adams, R.R., Tavares, A.A., Salzberg, A., Bellen, H.J., and Glover, D.M. (1998). *pavarotti* encodes a kinesin-like protein required to organize the central spindle and contractile ring for cytokinesis. Genes Dev. *12*, 1483–1494.

Adriaans, I.E., Basant, A., Ponsioen, B., Glotzer, M., and Lens, S.M.A. (2019). PLK1 plays dual roles in centralspindlin regulation during cytokinesis. J. Cell Biol. *218*, 1250–1264.

Basant, A., Lekomtsev, S., Tse, Y.C., Zhang, D., Longhini, K.M., Petronczki, M., and Glotzer, M. (2015). Aurora B kinase promotes cytokinesis by inducing centralspindlin oligomers that associate with the plasma membrane. Dev. Cell *33*, 204–215.

Basto, R., Lau, J., Vinogradova, T., Gardiol, A., Woods, C.G., Khodjakov, A., and Raff, J.W. (2006). Flies without centrioles. Cell *125*, 1375–1386.

Basto, R., Brunk, K., Vinadogrova, T., Peel, N., Franz, A., Khodjakov, A., and Raff, J.W. (2008). Centrosome amplification can initiate tumorigenesis in flies. Cell *133*, 1032–1042.

Berdnik, D., and Knoblich, J.A. (2002). *Drosophila* Aurora-A is required for centrosome maturation and actin-dependent asymmetric protein localization during mitosis. Curr. Biol. *12*, 640–647.

Bischof, J., Björklund, M., Furger, E., Schertel, C., Taipale, J., and Basler, K. (2013). A versatile platform for creating a comprehensive UAS-ORFeome library in *Drosophila*. Development *140*, 2434–2442.

Bringmann, H., and Hyman, A.A. (2005). A cytokinesis furrow is positioned by two consecutive signals. Nature *436*, 731–734.

Buster, D.W., Zhang, D., and Sharp, D.J. (2007). Poleward tubulin flux in spindles: regulation and function in mitotic cells. Mol. Biol. Cell *18*, 3094–3104.

Cabernard, C., Prehoda, K.E., and Doe, C.Q. (2010). A spindle-independent cleavage furrow positioning pathway. Nature *467*, 91–94.

Canman, J.C., Cameron, L.A., Maddox, P.S., Straight, A., Tirnauer, J.S., Mitchison, T.J., Fang, G., Kapoor, T.M., and Salmon, E.D. (2003). Determining the position of the cell division plane. Nature *424*, 1074–1078.

Caous, R., Pascal, A., Romé, P., Richard-Parpaillon, L., Karess, R., and Giet, R. (2015). Spindle assembly checkpoint inactivation fails to suppress neuroblast tumour formation in aurA mutant *Drosophila*. Nat. Commun. *6*, 8879.

Claret, S., Jouette, J., Benoit, B., Legent, K., and Guichet, A. (2014). PI(4,5)P2 produced by the PI4P5K SKTL controls apical size by tethering PAR-3 in *Drosophila* epithelial cells. Curr. Biol. *24*, 1071–1079.

Connell, M., Cabernard, C., Ricketson, D., Doe, C.Q., and Prehoda, K.E. (2011). Asymmetric cortical extension shifts cleavage furrow position in *Drosophila* neuroblasts. Mol. Biol. Cell *22*, 4220–4226.

Cullen, C.F., Deák, P., Glover, D.M., and Ohkura, H. (1999). *mini spindles*: A gene encoding a conserved microtubule-associated protein required for the integrity of the mitotic spindle in *Drosophila*. J. Cell Biol. *146*, 1005–1018.

D'Avino, P.P., Savoian, M.S., and Glover, D.M. (2005). Cleavage furrow formation and ingression during animal cytokinesis: a microtubule legacy. J. Cell Sci. *118*, 1549–1558.

D'Avino, P.P., Giansanti, M.G., and Petronczki, M. (2015). Cytokinesis in animal cells. Cold Spring Harb. Perspect. Biol. *7*, a015834.

Dietzl, G., Chen, D., Schnorrer, F., Su, K.C., Barinova, Y., Fellner, M., Gasser, B., Kinsey, K., Oppel, S., Scheiblauer, S., et al. (2007). A genome-wide transgenic RNAi library for conditional gene inactivation in *Drosophila*. Nature *448*, 151–156.

Edzuka, T., and Goshima, G. (2019). *Drosophila* kinesin-8 stabilizes the kinetochore-microtubule interaction. J. Cell Biol. *218*, 474–488.

Foe, V.E., and von Dassow, G. (2008). Stable and dynamic microtubules coordinately shape the myosin activation zone during cytokinetic furrow formation. J. Cell Biol. *183*, 457–470.

Fox, J.C., Howard, A.E., Currie, J.D., Rogers, S.L., and Slep, K.C. (2014). The XMAP215 family drives microtubule polymerization using a structurally diverse TOG array. Mol. Biol. Cell *25*, 2375–2392.

Gallaud, E., Caous, R., Pascal, A., Bazile, F., Gagné, J.P., Huet, S., Poirier, G.G., Chrétien, D., Richard-Parpaillon, L., and Giet, R. (2014). Ensconsin/Map7 promotes microtubule growth and centrosome separation in *Drosophila* neural stem cells. J. Cell Biol. *204*, 1111–1121.

Gervais, L., Claret, S., Januschke, J., Roth, S., and Guichet, A. (2008). PIP5K-dependent production of PIP2 sustains microtubule organization to establish polarized transport in the *Drosophila* oocyte. Development *135*, 3829–3838.

Glotzer, M. (2017). Cytokinesis in metazoa and fungi. Cold Spring Harb. Perspect. Biol. *9*, a022343.

Goshima, G., and Vale, R.D. (2005). Cell cycle-dependent dynamics and regulation of mitotic kinesins in *Drosophila* S2 cells. Mol. Biol. Cell *16*, 3896–3907.

Goshima, G., Wollman, R., Stuurman, N., Scholey, J.M., and Vale, R.D. (2005). Length control of the metaphase spindle. Curr. Biol. *15*, 1979–1988.

Hyman, A., Drechsel, D., Kellogg, D., Salser, S., Sawin, K., Steffen, P., Wordeman, L., and Mitchison, T. (1991). Preparation of modified tubulins. Methods Enzymol. *196*, 478–485.

Inoue, Y.H., Savoian, M.S., Suzuki, T., Máthé, E., Yamamoto, M.T., and Glover, D.M. (2004). Mutations in orbit/mast reveal that the central spindle is comprised of two microtubule populations, those that initiate cleavage and those that propagate furrow ingression. J. Cell Biol. *166*, 49–60.

Januschke, J., and Gonzalez, C. (2008). *Drosophila* asymmetric division, polarity and cancer. Oncogene *27*, 6994–7002.

Jordan, P., and Karess, R. (1997). Myosin light chain-activating phosphorylation sites are required for oogenesis in *Drosophila*. J. Cell Biol. *139*, 1805–1819.

Kaltschmidt, J.A., Davidson, C.M., Brown, N.H., and Brand, A.H. (2000). Rotation and asymmetry of the mitotic spindle direct asymmetric cell division in the developing central nervous system. Nat. Cell Biol. *2*, 7–12.

Knoblich, J.A. (2010). Asymmetric cell division: recent developments and their implications for tumour biology. Nat. Rev. Mol. Cell Biol. *11*, 849–860.

Kotýnková, K., Su, K.C., West, S.C., and Petronczki, M. (2016). Plasma membrane association but not midzone recruitment of RhoGEF ECT2 is essential for cytokinesis. Cell Rep. *17*, 2672–2686.

Laycock, J.E., Savoian, M.S., and Glover, D.M. (2006). Antagonistic activities of Klp10A and Orbit regulate spindle length, bipolarity and function *in vivo*. J. Cell Sci. *119*, 2354–2361.

Lee, M.J., Gergely, F., Jeffers, K., Peak-Chew, S.Y., and Raff, J.W. (2001). Msps/XMAP215 interacts with the centrosomal protein D-TACC to regulate microtubule behaviour. Nat. Cell Biol. *3*, 643–649.

Mathieu, J., Cauvin, C., Moch, C., Radford, S.J., Sampaio, P., Perdigoto, C.N., Schweisguth, F., Bardin, A.J., Sunkel, C.E., McKim, K., et al. (2013). Aurora B and cyclin B have opposite effects on the timing of cytokinesis abscission in *Drosophila* germ cells and in vertebrate somatic cells. Dev. Cell *26*, 250–265.

Mennella, V., Rogers, G.C., Rogers, S.L., Buster, D.W., Vale, R.D., and Sharp, D.J. (2005). Functionally distinct kinesin-13 family members cooperate to regulate microtubule dynamics during interphase. Nat. Cell Biol. *7*, 235–245.

Métivier, M., Monroy, B.Y., Gallaud, E., Caous, R., Pascal, A., Richard-Parpaillon, L., Guichet, A., Ori-McKenney, K.M., and Giet, R. (2019). Dual control of kinesin-1 recruitment to microtubules by Ensconsin in *Drosophila* neuroblasts and oocytes. Development *146*, dev171579.

Minestrini, G., Máthé, E., and Glover, D.M. (2002). Domains of the Pavarotti kinesin-like protein that direct its subcellular distribution: effects of mislocalisation on the tubulin and actin cytoskeleton during *Drosophila* oogenesis. J. Cell Sci. *115*, 725–736.

Minestrini, G., Harley, A.S., and Glover, D.M. (2003). Localization of Pavarotti-KLP in living *Drosophila* embryos suggests roles in reorganizing the cortical cytoskeleton during the mitotic cycle. Mol. Biol. Cell *14*, 4028–4038.

Mishima, M. (2016). Centralspindlin in Rappaport's cleavage signaling. Semin. Cell Dev. Biol. *53*, 45–56.

Morales-Mulia, S., and Scholey, J.M. (2005). Spindle pole organization in *Drosophila* S2 cells by dynein, abnormal spindle protein (Asp), and KLP10A. Mol. Biol. Cell *16*, 3176–3186.

Murthy, K., and Wadsworth, P. (2008). Dual role for microtubules in regulating cortical contractility during cytokinesis. J. Cell Sci. *121*, 2350–2359.

Radford, S.J., Harrison, A.M., and McKim, K.S. (2012). Microtubule-depolymerizing kinesin KLP10A restricts the length of the acentrosomal meiotic spindle in *Drosophila* females. Genetics *192*, 431–440.

Ramirez-Rios, S., Serre, L., Stoppin-Mellet, V., Prezel, E., Vinit, A., Courriol, E., Fourest-Lieuvin, A., Delaroche, J., Denarier, E., and Arnal, I. (2017). A TIRF microscopy assay to decode how tau regulates EB's tracking at microtubule ends. Methods Cell Biol. *141*, 179–197.

Rappaport, R. (1971). Cytokinesis in animal cells. Int. Rev. Cytol. *31*, 169–213.

Reber, S.B., Baumgart, J., Widlund, P.O., Pozniakovsky, A., Howard, J., Hyman, A.A., and Jülicher, F. (2013). XMAP215 activity sets spindle length by controlling the total mass of spindle microtubules. Nat. Cell Biol. *15*, 1116–1122.

Rebollo, E., Sampaio, P., Januschke, J., Llamazares, S., Varmark, H., and González, C. (2007). Functionally unequal centrosomes drive spindle orientation in asymmetrically dividing *Drosophila* neural stem cells. Dev. Cell *12*, 467–474.

Roth, M., Roubinet, C., Iffländer, N., Ferrand, A., and Cabernard, C. (2015). Asymmetrically dividing *Drosophila* neuroblasts utilize two spatially and temporally independent cytokinesis pathways. Nat. Commun. *6*, 6551.

Roubinet, C., Tsankova, A., Pham, T.T., Monnard, A., Caussinus, E., Affolter, M., and Cabernard, C. (2017). Spatio-temporally separated cortical flows and spindle geometry establish physical asymmetry in fly neural stem cells. Nat. Commun. *8*, 1383.

Royou, A., Sullivan, W., and Karess, R. (2002). Cortical recruitment of nonmuscle myosin II in early syncytial *Drosophila* embryos: its role in nuclear axial expansion and its regulation by Cdc2 activity. J. Cell Biol. *158*, 127–137.

Rueden, C.T., Schindelin, J., Hiner, M.C., DeZonia, B.E., Walter, A.E., Arena, E.T., and Eliceiri, K.W. (2017). ImageJ2: ImageJ for the next generation of scientific image data. BMC Bioinformatics *18*, 529.

Rusan, N.M., and Peifer, M. (2007). A role for a novel centrosome cycle in asymmetric cell division. J. Cell Biol. *177*, 13–20.

Shannon, K.B., Canman, J.C., Ben Moree, C., Tirnauer, J.S., and Salmon, E.D. (2005). Taxol-stabilized microtubules can position the cytokinetic furrow in mammalian cells. Mol. Biol. Cell *16*, 4423–4436.

Strickland, L.I., Donnelly, E.J., and Burgess, D.R. (2005). Induction of cytokinesis is independent of precisely regulated microtubule dynamics. Mol. Biol. Cell *16*, 4485–4494.

Sung, H.H., Telley, I.A., Papadaki, P., Ephrussi, A., Surrey, T., and Rørth, P. (2008). *Drosophila* Ensconsin promotes productive recruitment of kinesin-1 to microtubules. Dev. Cell *15*, 866–876.

Tsankova, A., Pham, T.T., Garcia, D.S., Otte, F., and Cabernard, C. (2017). Cell polarity regulates biased myosin activity and dynamics during asymmetric cell division via *Drosophila* Rho kinase and protein kinase N. Dev. Cell *42*, 143–155.e5.

Vale, R.D., Spudich, J.A., and Griffis, E.R. (2009). Dynamics of myosin, microtubules, and kinesin-6 at the cortex during cytokinesis in *Drosophila* S2 cells. J. Cell Biol. *186*, 727–738.

Verma, V., and Maresca, T.J. (2019). Microtubule plus-ends act as physical signaling hubs to activate RhoA during cytokinesis. eLife *8*, e38968.

Vernì, F., Somma, M.P., Gunsalus, K.C., Bonaccorsi, S., Belloni, G., Goldberg, M.L., and Gatti, M. (2004). Feo, the *Drosophila* homolog of PRC1, is required for central-spindle formation and cytokinesis. Curr. Biol. *14*, 1569–1575.

von Dassow, G. (2009). Concurrent cues for cytokinetic furrow induction in animal cells. Trends Cell Biol. *19*, 165–173.

Wang, H., Brust-Mascher, I., and Scholey, J.M. (2015). The microtubule cross-linker Feo controls the midzone stability, motor composition, and elongation of the anaphase B spindle in *Drosophila* embryos. Mol. Biol. Cell *26*, 1452–1462.

Widmann, T.J., and Dahmann, C. (2009). Dpp signaling promotes the cuboidal-to-columnar shape transition of *Drosophila* wing disc epithelia by regulating Rho1. J. Cell Sci. *122*, 1362–1373.

STAR★METHODS

KEY RESOURCES TABLE

REAGENT or RESOURCE	SOURCE	IDENTIFIER
Antibodies		
Rabbit polyclonal anti-PKCζ (C-20)	Santa Cruz (discontinued)	RRID:AB_2268962
Rabbit polyclonal anti-phospho histone H3 (ser10)	Millipore	RRID:AB_565299
Mouse DM1A monoclonal anti-α-tubulin	Sigma	RRID:AB_2617116
Mouse anti-Prospero	Developmental Studies Hybridoma Bank	RRID:AB_528440
Rabbit polyclonal anti-actin	Santa Cruz (discontinued)	Cat#sc-1616-R
Rabbit polyclonal anti-Klp10A	Gregory Rogers Lab; (Mennella et al., 2005)	PMID: 15723056
Rabbit polyclonal anti-Fasceto	Jonathan Scholey Lab; (Wang et al., 2015)	PMID: 25694445
Rabbit polyclonal anti-Msps	Jordan Raff Lab; (Lee et al., 2001)	PMID: 11433296
Rat monoclonal anti-Miranda	Abcam	Cat#ab197788
Rat Monoclonal anti-Deadpan	Abcam	RRID:AB_2687586
Rabbit polyclonal anti-Myosin	Roger Karess Lab; (Jordan and Karess, 1997)	PMID: 9412474
Chemicals, peptides, and recombinant proteins		
Colchicine	Sigma	C3915
Experimental models: Organisms/strains		
w ; Ubi-RFP-α-tubulin	Renata Basto Lab; (Basto et al., 2008)	PMID: 18555779
w ; Ubi-Sqh-GFP	Roger Karess Lab; (Royou et al., 2002)	PMID: 12105185
w ; UASp-GFP-Pav	David Glover Lab; (Minestrini et al., 2003)	PMID: 14517316
w ; Ubi-Feo-GFP	Bloomington *Drosophila* Stock center, (Wang et al., 2015)	RRID:BDSC_59273
w ; Inscuteable-Gal4	Bloomington *Drosophila* Stock center	RRID:BDSC_8751
w ; ;Ubi-PH-PLCδ-GFP	Antoine Guichet Lab; (Claret et al., 2014)	PMID: 24768049
w ; Ubi-PH-PLCδ-RFP	Antoine Guichet Lab; (Gervais et al., 2008)	PMID: 18948416
w ; Inscuteable-Gal4 ; UAS-mCherry-α-Tub	Bloomington *Drosophila* Stock center	RRID:BDSC_25773
w ; 69B-Gal4	Bloomington *Drosophila* Stock center	RRID:BDSC_1774
w ; ;UAS-Klp67A	FlyORF	F001232
w ; ;UAS-Klp10A	Christian Dahmann Lab; (Widmann and Dahmann, 2009)	PMID: 19366729
w ; ;UAS-Klp67A-RNAi	Vienna *Drosophila* Resource Center	VDRC ID 52105
w ; UAS-Feo-RNAi	Vienna *Drosophila* Resource Center	VDRC ID 52105
w ; ;UASt-Ensconsin-Venus	Régis Giet Lab; (Métivier et al., 2019)	PMID: 30936181
w ; UAS-Mad2 RNAi	Vienna *Drosophila* Resource Center	VDRC ID 106003
w; UASt-Msps-RFP	This study	
w; UAS-mCherry-α-tubulin	Bloomington *Drosophila* Stock center	RRID:BDSC_25774
w; UAS-mCherry-α-tubulin	Bloomington *Drosophila* Stock center	RRID:BDSC_25773
w; ;sas-4^{s2214}/TM6b	Bloomington *Drosophila* Stock center; (Basto et al., 2006)	RRID:BDSC_12119
w; pav^{b200}/TM6b	Anne Royou Lab; (Adams et al., 1998)	PMID: 9585508
w; svv^{2180}/Cyo	Jean-René Huynh Lab; (Mathieu et al., 2013)	PMID: 23948252
w ; ; *ensc ΔN*/TM6B	Pernille Rorth Lab; (Sung et al., 2008)	PMID: 19081075
w ; ; *ensc Δnull/TM6b*	Pernille Rorth Lab; (Sung et al., 2008)	PMID: 19081075
Oligonucleotides		
Fwd: 5′*ggggacaagtttgtac aaa aaa gca ggc t*ac aca ATG gcc gag gac aca gag tac aag aag 3′	This study	N/A
Rev: 5′*ggggaccactttgtaca a gaa agc tgg gt*t ATA ttg ggc atg att ctc ttt ctt gat ttg agc 3′	This study	N/A

(*Continued on next page*)

Continued

REAGENT or RESOURCE	SOURCE	IDENTIFIER
Recombinant DNA		
pDONR221-Msps	This study	N/A
pTWR	*Drosophila* Genomic Resource Center	Stock number 1136
pUASt-Msps-RFP	This study	N/A
Software and algorithms		
Fiji	fiji.sc	N/A
Prism version 7	GraphPad	N/A

RESOURCE AVAILABILITY

Lead contact

Further information and requests for reagents generated in this study should be directed to and will be fulfilled by the Lead Contact, Régis Giet (regis.giet@univ-rennes1.fr).

Materials availability

All unique/stable reagents generated in this study are available from the lead contact without restriction.

Data and code availability

- All data reported in this paper will be shared by the lead contact upon request.
- This paper study does not report original code.
- Any additional information required to reanalyze the data reported in this work paper is available from the Lead Contact upon request.

EXPERIMENTAL MODELS AND SUBJECT DETAILS

All flies were maintained under standard conditions at 25°C. The *ensconsin* mutant fly stocks *ensc*Δ*null* and *ensc*Δ*N*, referred to *ensc* flies, were characterized previously (Gallaud et al., 2014). UAS-Ensconsin-Venus transgenic flies have been characterized in a previous study (Métivier et al., 2019). UAS-Msps-RFP overexpressing flies were obtained from BestGene (USA) following P-element mediated transformation. UAS-Klp10A flies were supplied by C. Dahmann (Max Planck Institute, Germany) (Widmann and Dahmann, 2009). UAS-Klp67A (ID # F001232) stock was obtained from FlyORF (Bischof et al., 2013). UAS-Klp67A-RNAi (VDRC ID 52105) and UAS-Mad2-RNAi (VDRC ID 106003) transgenic fly lines were obtained from the Vienna *Drosophila* RNAi Center (Dietzl et al., 2007). Sqh-GFP (Royou et al., 2002), UAS-GFP-Pav-klp (Minestrini et al., 2003) and Ubiquitin-β-tub-GFP expressing flies (Inoue et al., 2004; Minestrini et al., 2003) were supplied by R. Karess (Institut Jacques Monod, France) and by D. Glover (University of Cambridge, UK), respectively. The Pavarotti mutant pav^{B200} flies were obtained from E. Montembault (Institut Européen de Chimie et Biologie, France) (Adams et al., 1998) and the Survivin mutant allele svn^{2180} flies were courtesy of Jean-René Hyunh (College de France, France) (Mathieu et al., 2013). Flies expressing the membrane-localized PH-PLCδ-GFP and PH-PLCδ-RFP proteins were provided by A. Guichet (Institut Jacques Monod, France) (Claret et al., 2014; Gervais et al., 2008). RFP-Tubulin flies were provided by R. Basto (Institut Currie, France). The GFP-AurA expressing fly stock was described previously (Caous et al., 2015). The following stocks were obtained from the Bloomington Stock Center: Feo-GFP expressed under the ubiquitin promoter (BDSC 59273, (Wang et al., 2015)), $sas\text{-}4^{s2214}$ mutant (BDSC 12119, (Basto et al., 2006)), 69B-Gal4 (BDSC 1774), Insc-Gal4 (BDSC 8751), UAS-mCherry-α-tubulin (BDSC 25774 and BDSC 25773). The *Feo* RNAi stock was from the Vienna *Drosophila* RNAi Center (VDRC 107824). The 69B-Gal4 fly stock was used to drive overexpression in the fly CNS for the following UAS regulated transgenes: Klp67A, Msps, GFP-Pav-Klp together with *Mad2* RNAi and UAS-mCherry at 25°C for 3 days and 2 days at 29°C for *Feo* RNAi. The Insc-Gal4 strain was used to drive overexpression of Ensconsin, Klp10A, UAS-GFP-Pav-klp and mCherry-α−tubulin transgenes in the central brain at 25°C.

METHOD DETAILS

Molecular biology

Msps cDNA was provided by G. Rogers (University of Arizona, USA), amplified by PCR and inserted into pDONR221 (Life Technologies) to generate the pDONR221-Msps entry clone. pENTR-Ensc has been previously described (Gallaud et al., 2014). pDONR221-Msps entry clone was subsequently recombined into pTWR (Carnegie Institute, USA) using the Gateway recombination

cloning technology (Life Technologies) to generate a construct allowing the expression of Msps-RFP fusion proteins under the control of the GAL4 protein. pENTR-Ensc was recombined into pDEST-MBP (a gift from H. Ohkura, University of Edinburgh, UK) to allow the expression of a recombinant Ensconsin protein with a C-terminal Maltose Binding Protein tag.

Production of recombinant proteins

MBP and Ensconsin-MBP were induced in *E. coli*, for 4 h at 25°C. The proteins were purified on amylose columns as described by the manufacturer (BioLabs) and stored in small aliquots at −80°C.

TIRF microscopy and analysis of MT dynamics

Tubulin was purified from bovine brain and fluorescently labeled with ATTO 488 and ATTO 565 or biotinylated as described before (Hyman et al., 1991; Ramirez-Rios et al., 2017). Briefly, microtubule seeds were prepared from biotinylated and ATTO-565-labeled tubulin in the presence of Guanosine-5′-[(α,β)-methyleno]triphosphate (GMPCPP) in BRB80 buffer (80 mM Pipes, 1 mM EGTA, 1 mM $MgCl_2$, pH 6.74) (Ramirez-Rios et al., 2017). Flow chambers were prepared with functionalized silane-PEG-biotin coverslips and silane-PEG glass slides, as previously described (Ramirez-Rios et al., 2017). The chamber was successively perfused at room temperature with neutravidin (25 μg/ml in 1% BSA in BRB80), PLL-g-PEG (2 kD, 0.1 mg/ml in 10 mM HEPES, pH 7.4), BSA (1% in BRB80 buffer) and microtubule seeds. The following assembly mixture was then injected: 14 μM tubulin (containing 15% ATTO-488-labeled tubulin) without or with 200 nM MBP or MBP-Ensconsin in TIRF assay buffer (4 nM DTT, 50 mM KCl, 1% BSA, 1 mg/mL glucose, 70 μg/mL catalase, 580 μg/mL glucose oxidase, 0.05% methylcellulose (4000 centipoise) in BRB80). Time-lapse images were recorded at 35°C at a rate of one frame per 5 s on an inverted Eclipse Ti Nikon microscope equipped with an Apochromat 60X1.49 N.A oil immersion objective, an iLas^2 TIRF system (Roper Scientific), and a cooled charge-coupled device camera (EMCCD Evolve 512, Photometrics) controlled by MetaMorph 7.7.5 software.

Microtubule dynamic parameters were analyzed in ImageJ on kymographs obtained using an in-house KymoTool macro (available upon request to eric.denarier@univ-grenoble-alpes.fr). Growth and shrinkage rates were determined from the slopes of microtubule growth and shrinkage phases. The catastrophe and rescue frequencies were calculated by dividing the number of events per microtubule by the time spent in growing and shrinking states, respectively.

Antibodies and western blotting

The following antibodies and concentrations were used in this study: polyclonal rabbit anti-Msps (1:5000) provided by J. Raff (Lee et al., 2001), polyclonal rabbit anti-Klp67A (1:500) supplied by G. Goshima (Goshima and Vale, 2005), polyclonal rabbit anti-Feo antibody (1:2000) was provided by J. Scholey (Wang et al., 2015), polyclonal rabbit anti-Klp10A (1:1000) was courtesy of G. Rogers (Mennella et al., 2005) and rabbit anti-Myosin (1:2000) was provided by R. Karess (Jordan and Karess, 1997). The anti-Ensconsin antibody raised against the Kinesin binding domain has been previously described (Gallaud et al., 2014). Rabbit anti-PKCζ (C-20, 1:200) and anti-actin polyclonal antibodies (sc-1616, 1:5000) were obtained from Santa Cruz Technology. Monoclonal mouse anti-alpha Tubulin (clone DM1A, T2199; 1:500) and rabbit polyclonal anti-phosphorylated histone H3 (Ser10) (06570, 1:500) antibodies were obtained from Millipore. Monoclonal rat anti-Miranda antibody (ab197788, 1:1000) was obtained from Abcam. Rat anti-Deapan (AB195173, 1:100) and mouse anti-Propero (MR1A, 1:500) antibodies were from DSHB. Secondary antibodies were labeled with either Alexa Fluor-conjugated (1:1000) or peroxidase-conjugated secondary antibodies (1:5000), each obtained from Life Technologies. For Western Blotting ECL reagents were purchased from ThermoFisher.

Live-cell microscopy

Third-instar larval brains were dissected in Schneider's *Drosophila* medium supplemented with 10% FCS. Isolated brains were loaded and mounted on stainless steel slides, and the preparations were sealed with mineral oil (Sigma-Aldrich) as previously described (Gallaud et al., 2014). For MT depolymerization experiments, larval brains were incubated during 30 min in the above medium supplemented with colchicine at a final concentration of 15 μM. After incubation, brains were mounted and processed for live cell imaging.

Images were acquired at 25°C using a CSU-X1 spinning-disk system mounted on an inverted microscope (Elipse Ti; Nikon) equipped with a 60X 1.4 NA objective. At 20, 30 or 60 s intervals 10 z-steps were acquired with 1μm intervals. Fluorescent protein probes were excited with 488nm or 561nm laser light and the images were captured using a sCMOS ORCA-Flash4.0 (Hamamatsu) camera. Recordings were controlled using MetaMorph acquisition software. Alternatively, images were acquired with a spinning disk system consisting of a DMi8 microscope (Leica) equipped with a 63X (1.4 N.A.) oil objective, a CSU-X1 spinning disk unit (Yokogawa) and an Evolve EMCCD camera (Photometrics). The microscope was controlled by the Inscoper Imaging Suite and the dedicated software (Inscoper). Data were processed in ImageJ and viewed as maximum-intensity projections prior to analysis or figure preparation.

Photo-ablation experiments

Photo-ablations were performed with a Mai-Tai two-photon infrared laser (Spectra Physics) attached to a Leica SP5 confocal microscope equipped with a 60X 1.3 NA objective with the stage maintained at 25°C. *Z*-series consisting of 10, 1μm steps were acquired before and after the photo-ablation at 30 s intervals. Photo-ablation was performed on the basal and apical centrosomes using flies expressing GFP-H2A, PH-PLCδ-GFP and Aurora A-GFP. Anaphase onset was identified as the first signs of sister chromatid

separation. The rapid (< 10 s, (Berdnik and Knoblich, 2002)) recovery of Aurora A-GFP was used to differentiate between centrosome photo bleaching and photo-ablation. Photo-ablation efficacy was confirmed using cells co-expressing RFP-tubulin. Cells that did not recovery the Aurora A-GFP signal within 30 s post-irradiation also displayed a loss of the MT-aster as reveled in live and fixed cell analyses.

Live-cell imaging analysis

Measurements of fluorescence intensities, distances, mitotic spindle lengths and diameters of NB and GMC cells were performed with ImageJ software (Rueden et al., 2017). The Sqh-GFP analyses were done on the maximum projection of two optical sections (1 μm). The cortical GFP-Pav-klp intensity analyses on the furrow during anaphase were calculated as the mean normalized intensity signal between the two sides of the furrow on two optical sections (1 μm). Cell cycle duration was calculated as the time between two consecutive NEBD events. The polarity-dependent apical and basal clearings were calculated, as the time point after anaphase onset, when myosin disappeared from the apical and basal cortices respectively (Connell et al., 2011; Roubinet et al., 2017). NB cortex curvature analyses were performed according to previously defined methods (Tsankova et al., 2017). The furrow shift was determined as the distance between the first ingression site and final cleavage site. To quantify the Myosin-GFP furrows width; a segmented line was drawn along the NB half-cell cortex during anaphase and the GFP intensity profiles were quantified along this line using ImageJ. The furrow width was measured as the relative half-cell cortex length containing 60% of the maximum Sqh-GFP signal intensity. Cortical expansion analyses were performed as described previously (Connell et al., 2011). Detailed analyses are illustrated in Figure S2A.

Immunofluorescence analysis

Larval brains from each genotype were processed for immunofluorescence studies as described previously (Gallaud et al., 2014). Briefly, wandering third instar larval brains were dissected in testis buffer (TB: 183 mM KCL, 47 mM NaCl, 10 MM Tris, and 1 mM EDTA, pH 6.8) and brains were fixed for 20 minutes at 25°C in TBF (TB supplemented with 10% formaldehyde, and 0.01% Triton X-100). Brains were then washed twice in PBS for 15 minutes, and twice in PBS Triton X-100 0.1% for 15 minutes. The brains were first incubated for 60 minutes at 25°C in PBSTB (1% BSA), before incubation with secondary antibodies. The samples were observed with a SP5 confocal microscope (Leica) equipped with a 63X 1.4NA objective lens. Images are maximum intensity projections consisting of 4 optical sections acquired at 0.5 μm intervals. The central brain NB number was calculated as the number of deadpan positive cells and the percentages of euploid, aneuploid and polyploid cells were determined on brain squashed preparation as described before (Caous et al., 2015).

QUANTIFICATION AND STATISTICAL ANALYSIS

Quantification of peripheral MTs in fixed NBs during mid-anaphase

Z series were acquired every 0.2 μm using a LSM 880 confocal microscope with Airyscan (Zeiss) for telophase NBs. Images were then processed with the Zen software. Images were analyzed with ImageJ as maximum intensity projections (0.8 μm) consisting of 5 optical (0.2 μm) sections in the plane of the furrow.

Statistical analysis

Differences between datasets were assessed with Prism 7.0a software (GraphPad), either by non-parametric tests (Mann-Whitney) or parametric tests (Unpaired T). Non-significance (ns) threshold was when $p > 0.05$. Statistical details can be found in the figure legend, with each "n" representing a distinct neuroblast.